Structure and Dynamics of a β-Helical Antifreeze Protein[†,‡]

Margaret E. Daley,[#] Leo Spyracopoulos,[#] Zongchao Jia,[§] Peter L. Davies,[§] and Brian D. Sykes*[,#]

Department of Biochemistry, University of Alberta, Edmonton, Alberta T6G 2H7, Canada, and Department of Biochemistry, Queen's University, Kingston, Ontario K7L 3N6, Canada

Received December 6, 2001; Revised Manuscript Received February 25, 2002

ABSTRACT: Antifreeze proteins (AFPs) protect many types of organisms from damage caused by freezing. They do this by binding to the ice surface, which causes inhibition of ice crystal growth. However, the molecular mechanism of ice binding leading to growth inhibition is not well understood. In this paper, we present the solution structure and backbone NMR relaxation data of the antifreeze protein from the yellow mealworm beetle *Tenebrio molitor* (TmAFP) to study the dynamics in the context of structure. The full ^{15}N relaxation analysis was completed at two magnetic field strengths, 500 and 600 MHz, as well as at two temperatures, 30 and 5 °C, to measure the dynamic changes that occur in the protein backbone at different temperatures. TmAFP is a small, highly disulfide-bonded, right-handed parallel β-helix consisting of seven tandemly repeated 12-amino acid loops. The backbone relaxation data displays a periodic pattern, which reflects both the 12-amino acid structural repeat and the highly anisotropic nature of the protein. Analysis of the ^{15}N relaxation parameters shows that TmAFP is a well-defined, rigid structure, and the extracted parameters show that there is similar restricted internal mobility throughout the protein backbone at both temperatures studied. We conclude that the hydrophobic, rigid binding site may reduce the entropic penalty for the binding of the protein to ice. The β-helical fold of the protein provides this rigidity, as it does not appear to be a consequence of cooling toward a physiologically relevant temperature.

Various organisms, including many marine fishes (*1*), insects (*2*), and plants (*3*, *4*), use antifreeze proteins (AFPs),[1] also known as thermal hysteresis proteins, as a freeze avoidance strategy. For example, the yellow mealworm beetle *Tenebrio molitor* and the spruce budworm (*Choristoneura fumiferana*) produce AFP in their hemolymph to survive overwintering in the larval stage (*5*, *6*). Since their discovery in fish and insects more than 30 years ago (*7*, *8*), the biophysical properties of these proteins have inspired widespread interest. Their protective effect stems from their ability to bind to ice and thereby inhibit ice crystal growth. This interaction at the ice surface leads to a lowering of the nonequilibrium freezing point below the melting point, termed thermal hysteresis (for reviews, see refs *9* and *10*).

Even though it is well accepted that AFPs bind to ice and inhibit its growth, the actual mechanism of this binding is not well understood. In the past decade, the structures of numerous AFPs belonging to five different types have been solved, and none of these have any sequence or structural similarity to each other. In fish, type I AFP from winter flounder (*11*) is a single, long α-helix; type II AFP from sea raven has a homologous fold to the carbohydrate-recognition domain of Ca^{2+}-dependent lectin family of proteins (*12*); the eel pout type III AFP is a small β-sheet protein with a unique fold (*13*, *14*); while a model of a four-helix bundle structure for type IV AFP from the longhorn sculpin has been made based on its high degree of sequence homology with the exchangeable apolipoproteins (*15*). More recently, the structures of two β-helical insect AFPs (*Tenebrio molitor*, TmAFP, and spruce budworm, sbwAFP) were solved (*16*, *17*). These insect AFPs are much more potent than their fish counterparts. For type I, type III, and sbwAFP (and by analogy, TmAFP) putative ice-binding faces have been proposed based on mutation studies (*17*−*23*). The only feature these possible sites appear to have in common is that they are quite flat surfaces, and, in the case of type I and the insect AFPs, they have evenly spaced ranks of threonine that appear to match the ice lattice (*16*, *24*). For sbwAFP and TmAFP, the increased thermal hysteresis activity displayed by these proteins could be due to these proteins binding to two different planes of ice (*17*), a suggestion that has been made for the type III antifreeze protein as well (*14*).

[†] This work was supported through grants from the Canadian Institutes of Health Research (CIHR) to Z.J., P.L.D., and B.D.S., and from the Protein Engineering Network of Centres of Excellence to P.L.D. and B.D.S. M.E.D. is supported by a CIHR Doctoral Research Award.

[‡] The atomic coordinates (code 1L1I) have been deposited in the Protein Data Bank, Research Collaboratory for Structural Bioinformatics, Rutgers University, New Brunswick, NJ (http://www.rcsb.org/pdb/). The ^{1}H and ^{15}N chemical shift assignments have been deposited with accession number 5323 in the BioMagResBank, University of Wisconsin−Madison (http://www.bmrb.wisc.edu).

* To whom all correspondence should be addressed. Telephone: 780-492-5460. Fax: 780-492-0886. E-mail: brian.sykes@ualberta.ca.

[#] University of Alberta.

[§] Queen's University.

[1] Abbreviations: AFP, antifreeze protein; HNHA, ^{15}N-edited $^{1}H^{N}$-$^{1}H^{\alpha}$ correlation experiment; HNHB, ^{15}N-edited $^{1}H^{N}$-$^{1}H^{\beta}$ correlation experiment; HSQC, heteronuclear single quantum coherence; NMR, nuclear magnetic resonance; NOE, nuclear Overhauser enhancement; NOESY, nuclear Overhauser effect spectroscopy; rmsd, root-mean-square deviation; T_1, longitudinal relaxation time; T_2, transverse relaxation time; TOCSY, total correlation spectroscopy.

10.1021/bi0121252 CCC: $22.00
Published on Web 04/05/2002

Although structure often leads to insight into protein function, in this case, structures alone have not allowed elucidation of a molecular mechanism for antifreeze protein binding to ice. In attempts to understand this interaction more fully, we have moved to study protein dynamics in the context of structure. Protein dynamics studies have become an important tool in understanding the processes underlying molecular recognition and the relationship of structure and function. Using heteronuclear, multidimensional NMR spectroscopy it is possible to study the dynamics of individual nuclei in proteins in a site-specific manner. In particular, measurement of NMR relaxation of backbone amide ^{15}N nuclei provides detailed information regarding backbone motions of the protein (*25*). In many cases of protein−ligand complexes, it is the flexibility of the protein and the ligand, as well as the flexibility of the binding interface that determine the affinity of the interaction (*26*). In this case, the ligand in question is ice, and the interface cannot be fixed in solution, so we must use alternate methods to probe this binding interaction. Recently, Graether et al. (*27*) have shown that type I AFP remains structured and behaves predictably until the solution freezes at −3 °C. Similar experiments with TmAFP (Daley et al., unpublished) show that this AFP also does not denature under supercooling conditions and suggests that the native folded state is the active form. This is in contrast to the conformation and dynamics study of an antifreeze glycoprotein that appears to contain no permanent secondary structure and is active in its extended form (*28*). To our knowledge, these are the only dynamics studies on antifreeze and related proteins. It seems clear from this comparison that antifreeze proteins and glycoproteins have fundamentally different modes of action, and the latter will not be discussed further.

In this paper, we present the solution structure of the *T. molitor* antifreeze protein, along with its backbone NMR relaxation data. This is the first extensive study of backbone dynamics of any antifreeze protein. We have completed full ^{15}N relaxation analysis at two temperatures, 30 and 5 °C, to determine the type of dynamic changes that occur in the backbone conformation of TmAFP as the temperature is lowered toward its physiologically active level.

EXPERIMENTAL PROCEDURES

Sample Preparation. The expression and purification of both unlabeled and ^{15}N-labeled TmAFP was as previously described (*29*). The ^{15}N-TmAFP sample was prepared for NMR spectroscopy by dissolving lyophilized protein in 90% H_2O/10% D_2O containing 0.1 mM DSS (2,2-dimethylsilapentane-5-sulfonic acid). The final protein concentration was approximately 0.4 mM, and the pH was adjusted to 5.5 with microliter aliquots of 100 mM NaOD or DCl as required. The unlabeled TmAFP sample was prepared by dissolving the lyophilized protein in either 90% H_2O/10% D_2O or 100% D_2O as required. The final protein concentration was approximately 1 mM, with the pH adjusted to 5.5 and 0.1 mM DSS added.

Assignment. NMR spectra for ^{1}H and ^{15}N chemical shift assignment were acquired using a Varian Unity 600 MHz spectrometer equipped with a 5-mm triple resonance probe and *z*-axis pulsed field gradients. All spectra for assignment were collected at 30 °C. The spectral widths for ^{1}HN and ^{15}N were 7000.35 and 1897.89 Hz, respectively. Experiments

QCTGGADCTSCT
GACTGCGNCPNA
VTCTNSQHCVKA
NTCTGSTDCNTA
QTCTNSKDCFEA
NTCTDSTNCYKA
TACTNSSGCPGH

FIGURE 1: Amino acid sequence of the *T. molitor* AFP isoform used in this study. The repetitiveness of the sequence is highlighted by use of red for Cys, blue for Thr, light blue for Ser, and green for Ala. The underlined residues correspond to the regions of the protein that involve β-sheet secondary structure.

used for assignment were ^{15}N-HSQC with 448 (HN) and 128 (^{15}N) real data points acquired with a total of 256 transients per t_1 increment, ^{15}N-edited TOCSY with 420 (HN), 116 (H), and 30 (^{15}N) real data points acquired with a total of 36 transients per increment, HNHA with 448 (HN), 52 (H), and 52 (^{15}N) real data points acquired with a total of 40 transients per increment, and HNHB with 512 (HN), 96 (H), and 30 (^{15}N) real data points acquired with a total of 32 transients per increment. Sequential assignments were made using an ^{15}N-edited NOESY acquired on a Varian INOVA 800 MHz spectrometer equipped with a 5-mm triple resonance probe and *x*, *y*, and *z*-axis pulsed field gradients. The spectral widths for ^{1}HN, ^{1}H, and ^{15}N were 10000, 8200, and 2188.4 Hz, respectively. The numbers of real data points acquired were 640 (HN), 172 (H), and 32 (^{15}N) with a total of 16 transients per increment. The mixing time was 100 ms. Following sequential assignment, the two proline residues were assigned from the δCHs using a natural abundance ^{13}C-HSQC experiment with 448 (^{1}H) and 306 (^{13}C) real data points acquired with a total of 352 transients per increment. The lysine and glutamine side chains were then fully assigned using 2D TOCSY and NOESY experiments with 2048 (^{1}H) and 256 (^{1}H) real data points with a total of 64 transients per increment. The three previous experiments were collected at 600 MHz (spectral widths were 7000.35 Hz for ^{1}H and 2000 Hz for ^{13}C) on the unlabeled TmAFP sample in D_2O. Spectra were processed with NMRPipe (*30*) and analyzed using NMRView (*31*) programs.

Due to the repetitive sequence and structure of TmAFP, shown in Figure 1, the chemical shift assignment procedure used was atypical. Many residues are in similar environments in the protein and discrimination of chemical shifts was difficult. This was further complicated by the fact that NOEs between residues 12 amino acids apart in sequence were in many cases stronger than the sequential connections, which was misleading in the process of NOE assignment. These realizations were made once we analyzed the crystal structure of TmAFP (*16*). Using the PDB coordinates (prior to publication, 1EZG), we measured distances from the backbone amide proton to other protons in the protein and concluded that interloop distances were less than the sequential distances, since the secondary structure consists only of extended strands and turns. By thus correlating the interproton distances from the crystal structure with the NOE cross-peak intensities, a structure-specific sequential assign-

ment of TmAFP was completed, with full ^{1}H and ^{15}N chemical shift assignments made. The crystal structure itself was not directly used in the assignment process.

Structure Calculations. An ensemble of 50 TmAFP structures was generated from 672 distance restraints and 98 dihedral angle restraints using the simulated annealing program CNS version 1.0 (Crystallography & NMR System, *32*). Interproton distance restraints were obtained from the ^{15}N-edited NOESY with additional side chain NOE restraints obtained from the high-resolution homonuclear two-dimensional ^{1}H-^{1}H NOESY experiment. The ψ dihedral angle restraints were obtained from an analysis of the $^3J_{HN-HA}$ coupling constants measured in the 3D HNHA experiment (*33*). The ψ dihedral angle restraints were determined by analysis of $d_{N\alpha}/d_{\alpha N}$ ratios; however, these were incorporated with typically large bounds ($\pm$ 100°) and only in the regions of well-defined structure after initial structure calculations using NOE distance restraints (*34*). All structure calculations included the eight disulfide bonds, which were previously determined to have the following connectivities: Cys^2−Cys^{11}, Cys^8−Cys^{18}, Cys^{15}−Cys^{21}, Cys^{27}−Cys^{33}, Cys^{39}−Cys^{45}, Cys^{51}−Cys^{57}, Cys^{63}−Cys^{69}, Cys^{75}−Cys^{81} (*29*). The disulfide bonds were restrained to a distance of 2.02 $\pm$ 0.1 Å. No distance violations greater than 0.5 Å or dihedral angle violations greater than 5° were found. PROCHECK_NMR (*35*) was used to analyze the quality of the structures and VADAR (*36*) was used to assign secondary structure. Figures 3, 4, and 5 were generated using MOLSCRIPT (*37*) and Raster3D (*38*).

DYNAMICS

NMR Spectroscopy. NMR spectra were acquired using Varian INOVA 500 MHz and Unity 600 MHz spectrometers equipped with 5-mm triple resonance probes and *z*-axis pulsed field gradients. ^{15}N-T_1, -T_2, and {^{1}H}-^{15}N NOE experiments were carried out at 500 and 600 MHz at both 30 and 5 °C using sensitivity-enhanced gradient HSQC pulse sequences developed by Farrow et al. (*39*). For measurement of ^{15}N-T_1 relaxation times at 30 °C, delays of 11.1, 55.5, 122.1, 199.8, 277.5, 388.5, 499.5, 666, 888, and 1110 ms were used at 500 MHz and delays of 11.1, 55.5, 122.1, 199.8, 277.5, 388.5, 499.5, 666, 888, and 999 ms were used at 600 MHz. At 5 °C, delays of 11.1, 55.5, 122.1, 199.8, 277.5, 388.5, 499.5, 610.5, 721.5, 832.5, 888, and 999 ms were used at 500 MHz and delays of 11.1, 55.5, 122.1, 199.8, 277.5, 388.5, 499.5, 610.5, 777, and 999 ms were used at 600 MHz. For measurement of ^{15}N-T_2 relaxation times at both 30 and 5 °C, delays of 16.61, 33.22, 49.83, 66.44, 83.05, 99.66, 116.27, 132.88, 149.49, and 166.1 ms were used at 500 MHz. Delays of 16.544, 33.088, 49.632, 66.176, 82.72, 99.264, 115.808, 132.352, 148.896, and 165.44 ms were used at 600 MHz. To obtain equilibrium, a 1.0 s delay between repetitions of the pulse sequence for ^{15}N-T_1 measurements was employed, while the delay for obtaining equilibrium during the measurement of ^{15}N-T_2 was 2.5 s. {^{1}H}-^{15}N steady-state NOEs were measured from two HSQC spectra acquired with (NOE experiment) and without (noNOE experiment) proton saturation prior to the first ^{15}N excitation pulse. Proton saturation at both 500 and 600 MHz was achieved using a train of 120° proton pulses with 5 ms pulse intervals for a total 3.5 s of saturation. Relaxation delays of 2 ms (NOE experiment) or 5 ms (noNOE experiment) between repetitions of the pulse sequence were used. The spectral widths for ^{1}H and ^{15}N were 5500.172 and 1670.007 Hz at 500 MHz and 7000.35 and 2000 Hz at 600 MHz, respectively. The number of real data points acquired for ^{1}H and ^{15}N, respectively, were 352 and 96 (30 °C) or 128 (5 °C) at 500 MHz and 436 and 96 (30 °C) or 128 (5 °C) at 600 MHz. A total of 32 or 64 transients per t_1 increment were collected for ^{15}N-T_1 and -T_2 at 30 °C, while 48 or 52 transients were collected at 5 °C. At 500 MHz, 112 (30 °C) or 92 (5 °C) transients were accumulated for measurement of {^{1}H}-^{15}N NOE, while at 600 MHz, 96 transients were collected at both 30 and 5 °C.

NMR Data Processing. All NMR data were processed with the NMRPipe software (*30*). Enhanced sensitivity data were processed using the ranceY.M macro. The F_1 (^{15}N) dimension was extended by 32 complex points using linear prediction before zero filling. The F_2 (^{1}H) dimension was multiplied by a 60°-shifted sine-bell function and the F_1 dimension was multiplied by a 75°-shifted squared sine-bell function before Fourier transformation. The F_1 and F_2 dimensions were baseline corrected by polynomial subtraction in the frequency domain. At 5 °C, an additional window function was employed. The NMRView program (*31*) was used for peak picking of all {^{1}H-^{15}N}-HSQC spectra. The values of the peak intensities for the ^{15}N-T_1 and -T_2 measurements were fit to single-exponential, two-parameter decay curves using the xcrvfit program (software available at: http://www.pence.ca/ftp). Error in the ^{15}N-T_1 and -T_2 measurements was obtained from non-linear least-squares fits of the peak intensities to two-parameter exponential decays. Error in the {^{1}H}-^{15}N NOE values was calculated from baseplane noise values in ^{15}N-HSQC spectra acquired with and without proton saturation.

^{15}N-Relaxation Data Analysis. In general, the dipolar interaction between the ^{15}N nucleus and its attached proton and chemical shift anisotropy of the ^{15}N nucleus are the main contributions to the backbone amide T_1 and T_2 relaxation times and the ^{15}N-NOE enhancement (*40*). The theoretical expressions describing ^{15}N-T_1, -T_2, and {^{1}H}-^{15}N steady-state NOE relaxation parameters are given here as linear combinations of the appropriate spectral density functions:

$$\frac{1}{T_1} = D[J(\omega_H - \omega_N) + 3J(\omega_N) + 6J(\omega_H + \omega_N)] + C[J(\omega_N)] \quad (1)$$

$$\frac{1}{T_2} = \frac{D}{2}[4J(0) + J(\omega_H - \omega_N) + 3J(\omega_N) + 6J(\omega_H) + 6J(\omega_H + \omega_N)] + (1/6)C[3J(\omega_N) + 4J(0)] \quad (2)$$

$$\mathrm{NOE} = 1 + (\gamma_H/\gamma_N)D[6J(\omega_H + \omega_N) - J(\omega_H - \omega_N)]T_1 \quad (3)$$

where $D = (\mu_0/4\pi)^2(\gamma_H^2\gamma_N^2\hbar^2/4r_{NH}^6)$ and $C = \Delta^2\omega_N^2/3$, ω_H and ω_N are the Larmor frequencies of ^{1}H and ^{15}N, respectively, γ_H is the magnetogyric ratio of ^{1}H (2.68×10^8 rad s^{-1} T^{-1}), γ_N is the magnetogyric ratio of ^{15}N (-2.71×10^7 rad s^{-1} T^{-1}), μ_0 is the permeability constant of free space ($4\pi \times 10^{-7}$ kg m s^{-2} A^{-2}), $\hbar$ is Planck's constant divided by 2π (1.05×10^{-34} J s), r_{NH} is the nitrogen−proton

internuclear distance (1.02 Å), and Δ is the difference between the parallel and perpendicular components of the ^{15}N chemical shift tensor (−160 ppm). The spectral density function is represented with the Lipari-Szabo model-free formalism (*41*, *42*), using a generalized order parameter S^2, which describes the degree of spatial restriction of each backbone amide HN−N bond vector. With the assumption of isotropic tumbling of the molecule, a single, overall rotational correlation time for the protein, and an associated internal correlation time, the spectral density function is defined as:

$$J(\omega) = \frac{2}{5}\left[\frac{S^2\tau_m}{(1+\omega^2\tau_m^2)} + \frac{(1-S^2)\tau}{(1+\omega^2\tau^2)}\right] \quad (4)$$

where $\tau^{-1} = \tau_m^{-1} + \tau_e^{-1}$, with τ_m being the correlation time for overall molecular tumbling and τ_e the correlation time for internal motion. The relaxation data for each residue is then fit to a motional model describing the overall molecular tumbling of the protein, including one or two types of internal motions of various time-scales. For computational reasons, the basic motional model is separated into five specific models, as previously described (*39*). These models are tested iteratively starting with the simplest model, and subsequently the more complex models, until the proposed model describes the measured relaxation rates within 95% confidence limits. Model 1 uses a form of the function in eq 4, including the parameters S^2, describing the amplitude of the spatial restriction for each backbone amide vector varying from 0 (no spatial restriction) to 1 (complete spatial restriction), and τ_m. In model 1, it is assumed that τ_e is fixed at zero and does not contribute to relaxation. Model 2 includes S^2, τ_m, and τ_e, and it is assumed that the internal motions corresponding to τ_e are within the picosecond time-scale ($0 < \tau_e < \tau_m$) and contribute to the relaxation. Model 3 is a modification of model 1, which includes a parameter (R_{ex}, in s^{-1}) to describe the contribution of microsecond to millisecond time-scale internal motions to $1/T_2$. Model 4 is model 2 modified to include the R_{ex} parameter. Model 5 invokes internal motion occurring on two time-scales (*43*, *44*). It includes an order parameter (S^2_f) for picosecond time-scale internal motions, an order parameter (S^2_s) for nanosecond time-scale internal motions that are faster than τ_m but slower than τ_e, and a correlation time (τ_s) for nanosecond time-scale internal motions. The correlation time τ_e, for picosecond time-scale internal motions, is assumed not to contribute to the relaxation (as in model 1). The extended model spectral density function is given in eq 5:

$$J(\omega) = \frac{2}{5}\left[\frac{S^2\tau_m}{(1+\omega^2\tau_m^2)} + \frac{(S^2_f - S^2)\tau'_s}{(1+\omega^2\tau'^2_s)}\right] \quad (5)$$

where $S^2 = S^2_f S^2_s$ and $\tau'_s = \tau_s\tau_m/(\tau_s + \tau_m)$. To determine the most appropriate model to describe each residue, the parameters for each spectral density function are adjusted to minimize the following χ^2 function:

$$\chi^2 = \frac{(T_{1c} - T_{1e})^2}{\sigma^2_{T1}} + \frac{(T_{2c} - T_{2e})^2}{\sigma^2_{T2}} + \frac{(\mathrm{NOE_c} + \mathrm{NOE_e})^2}{\sigma^2_{\mathrm{NOE}}} \quad (6)$$

where the subscripts c and e indicate calculated and experimental values, respectively, and σ is the error of the individual relaxation parameters used.

In the case of rigid body anisotropic reorientation, the spectral density function has been fully detailed elsewhere (*45*, *46*), for example, in eqs 3 and 4 in the paper by Tjandra et al. (*46*). The six parameters (D_{xx}, D_{yy}, D_{zz}, θ, ϕ, and ψ) describing the orientation and amplitude of the principal components of the diffusion tensor in the molecular frame are optimized. The diffusion parameters are then extracted by minimizing the error function:

$$\chi^2 = \sum_n \{[(R_2^{meas}/R_1^{meas}) - (R_2^{calc}/R_1^{calc})]_n/\sigma_n\}^2 \quad (7)$$

where σ is the uncertainty in the experimental R_2/R_1 ratio. The summation is performed over all residues defined as rigid using the following equations as proposed by Tjandra et al. (*46*, *47*):

$$\mathrm{NOE} < \overline{\mathrm{NOE}} - 1.5\ \mathrm{SD} \quad (8a)$$

$$\frac{\langle T_2\rangle - T_{2,n}}{\langle T_2\rangle} - \frac{\langle T_1\rangle - T_{1,n}}{\langle T_1\rangle} > 1.5\ \mathrm{SD} \quad (8b)$$

where the T_1 and T_2 averages are taken over residues that have not been excluded because of a low NOE (eq 8a). SD is the standard deviation of the function calculated for these residues.

For the diffusion tensor and internal mobility analysis, the Cartesian coordinates of TmAFP were taken from the crystal structure. The fit of the components and orientation of the diffusion tensor is performed using an in-house written program (*48*) and visualized with the program TENSOR2 (*49*). The relaxation parameters are analyzed with respect to isotropic, axially symmetric, and fully asymmetric rotational tumbling models using TENSOR2. The significance of the improved fit of each model is tested to ensure that the reduction in χ^2 is not due only to the introduction of additional parameters into the each subsequently more complex model.

The global isotropic correlation time has been optimized using those residues that do not display obvious signs of relaxation active mobility, using the exclusion criteria detailed in eqs 8a and 8b above. With the assumption of negligible internal mobility and exchange, the T_1/T_2 ratios of these residues should be dependent only on the overall reorientation of the molecule.

With the orientation and the components of the diffusion tensor optimized using the selected vectors, the internal mobility, shown here for the case of axially symmetric rotational diffusion, is characterized using the spectral density function extended to include fast internal motions:

$$J(\omega) = \frac{2}{5}S^2_f\sum_{j=1}^{3}A_j\left\{\frac{S^2_s\tau_j}{1+(\omega\tau_j)^2} + \frac{(1-S^2_s)\tau'_j}{1+(\omega\tau'_j)^2}\right\} \quad (9)$$

with $\tau'_j = \tau_j\tau_s/(\tau_j + \tau_s)$, $\tau_1^{-1} = 6D_\perp$, $\tau_2^{-1} = 5D_\perp + D_{||}$, $\tau_3^{-1} = 2D_\perp + 4D_{||}$, $A_1 = (3\cos^2\theta - 1)^2/4$, $A_2 = 3\sin^2\theta\cos^2\theta$, $A_3 = (^3/_4)\sin^4\theta$, where θ is the angle between the NH bond vector and the unique axis of the principal frame of the

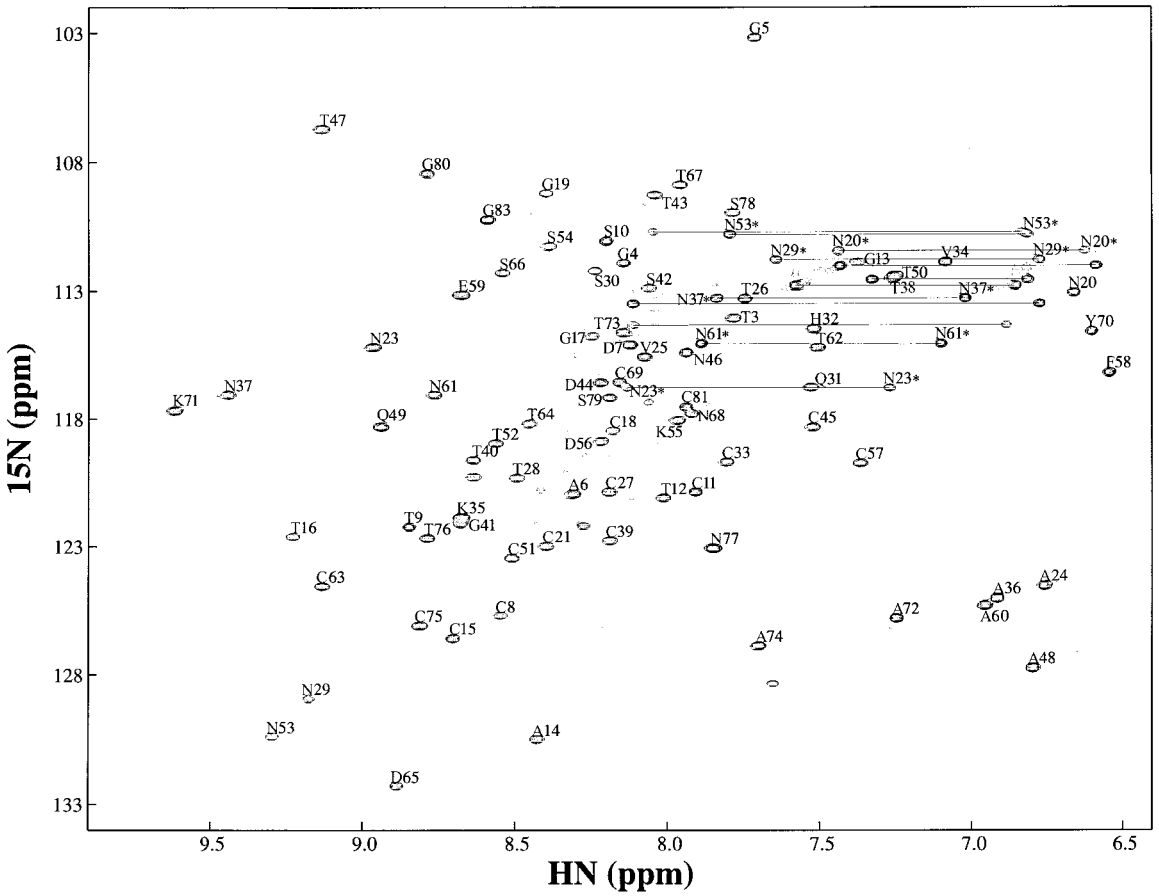

FIGURE 2: ^{1}H-^{15}N HSQC spectrum of TmAFP at 30 °C, showing the complete backbone amide assignments and the wide chemical shift dispersion.

diffusion tensor. This is analogous to the isotropic Lipari-Szabo formalism, as the fast internal motion ($\tau_j \ll (6D)^{-1}$) is assumed to be independent of the overall rotational tumbling. The statistical tests performed to determine the significance of the derived models use the same criteria for model selection as in the isotropic case described above.

RESULTS

Solution Structure of TmAFP. The recombinant TmAFP used in this study consists of 85 residues, with the N-terminal Met used to initiate translation in *E. coli* numbered 0. In this way, sequence numbering remains consistent with the native protein. The extreme regularity of the sequence and structure as well as the abundance of small amino acid side chains (Figure 1) made it very difficult to assign the ^{1}H and ^{15}N chemical shifts of this protein. Despite this, almost complete ^{1}H and ^{15}N NMR chemical shift assignments of TmAFP were obtained using the structure-specific assignment procedure discussed in the experimental procedures. Backbone amide protons were unambiguously assigned for 79 out of the 83 non-proline residues at both 30 °C (Figure 2) and 5 °C (not shown). Resonances for the N-terminal Met^{0}, Gln^{1}, and Cys^{2}, as well as the C-terminal His^{84} were not observed. As can be seen in the ^{1}H-^{15}N HSQC spectrum in Figure 2, the resonances are generally well-dispersed, and the spectra are of high resolution. In addition, complete assignment of all side chains resonances was accomplished, with the exception of the four residues mentioned above which were not observed, and the side chain amide groups of three asparagines and the three glutamines that could not be unambiguously distinguished.

Table 1: Structural Statistics for the Ensemble of 20 Refined Structures of TmAFP

	ensemble	selected structure
rmsd from NOE distances (Å) (672)	0.022 ± 0.001	0.021
rmsd from dihedral angle restraints (degrees) (98)	0.37 ± 0.11	0.396
rmsd from idealized covalent geometry		
bonds (Å)	0.0025 ± 0.0002	0.0022
angles (degrees)	0.37 ± 0.01	0.35
impropers (degrees)	0.23 ± 0.02	0.22
Cartesian coordinate rmsd (Å)		
backbone atoms (N, Cα, C)	0.8 ± 0.1	0.6
all heavy atoms	1.1 ± 0.1	1.0
Ramachandran plot analysis		
residues in most favored regions	53.3%	52.8%
residues in additionally allowed regions	45.2%	47.2%
residues in disallowed regions	1.5%	0%

Restraints for 672 interproton distances (148 long-range, ($|i - j| \geq 5$); 40 medium-range, ($2 \leq |i - j| \leq 4$); 202 sequential ($|i - j| = 1$) and 282 intraresidue ($i = j$) and 98 ϕ and ψ dihedral angles were derived as described in the experimental procedures. An ensemble of structures was generated using these restraints (Figure 3). The statistics for this ensemble are summarized in Table 1. Overall, the calculated structures exhibit good covalent geometry and agree well with the experimental data. The single structure

FIGURE 3: The tertiary structure of *T. molitor* antifreeze protein. Shown is the Cα trace of the superimposition (using residues 13−81) of the main chain atoms from the 20 lowest energy NMR-derived structures of TmAFP (PDB code 1L1I).

closest to the mean of the ensemble was selected for illustrative purposes and the following discussion.

TmAFP is a right-handed parallel β-helix consisting of seven repetitive 12-amino acid loops (Figure 4). The consensus sequence for these repeated loops is xTCTxSxxCxxA, as described previously (*50*) and shown in Figure 1. The overall shape of the protein is a flattened cylinder approximately 32 Å long, with a 14 × 8 Å pseudo-rectangular cross section. The structure is constrained by a series of intraloop disulfide bonds running through the middle of the helix core. All 16 cysteines in TmAFP are involved in these disulfide bridges. Six of the eight disulfide bonds are spaced 6 residues apart and are aligned in the center of each loop, except the N-terminal one (Figure 4). In the N-terminal region, the other two disulfide bonds (Cys^2−Cys^{11} and Cys^8−Cys^{18}) do not conform to this regular pattern; however, the N-terminal loop formation is not disrupted. The structure is further stabilized by a network of hydrogen bonds whose existence is supported by the observation of long-lived amide proton resonances in the two-dimensional TOCSY spectrum in D_2O. These hydrogen bonds are present in the β- and γ-turns of the individual helical loops, as well as in the stacking of adjacent loops (*16*). This is due to the extremely similar backbone conformations of each loop of the helix.

Due to the tightness of this β-helix, with only 12 residues per loop, TmAFP has essentially no hydrophobic core and certainly no room inside the helix for long side chains. In addition to the disulfide-bonded cysteines that bisect each loop, the only other residues that fit inside the core are the conserved alanine and serine residues that line the right and left-hand sides of the protein, respectively, for the view in Figure 4C. All the rest of the side chains, including the relatively few hydrophobic ones, project out into solution.

Each loop of the helix, except the N- and C-terminal ones, contributes a 3−4 residue β-strand to the sheet that is formed along one side of the protein. This sheet contains the array of threonine residues from the TCT motif that is the putative ice-binding face. The rest of the loop consists of extended coil structure as well as β- and γ-turns. The entire protein constitutes a well-defined structure, with rms distributions about the mean coordinate positions of 0.8 ± 0.1 Å for backbone atoms and 1.1 ± 0.1 Å for all heavy atoms from residues 13−81. The N-terminal 12 residues are poorly defined due to the smaller number of NOE restraints in this region.

This structure agrees very well with that previously determined by X-ray crystallography (*16*) (Figure 5). The rmsd between the representative solution structure and the X-ray structure is 1.3 Å for backbone atoms and 2.0 Å for

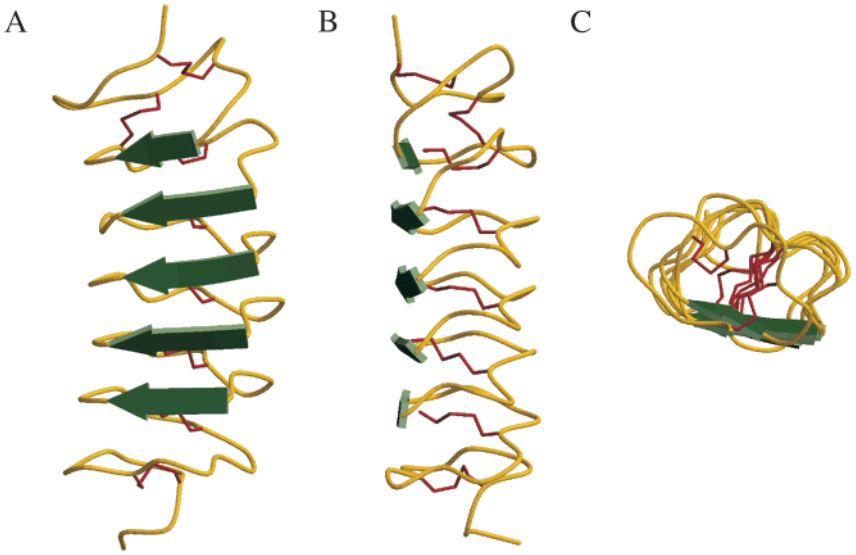

FIGURE 4: Ribbon representation of the TmAFP structure closest to the mean. The β-sheets, shown in green, are located at residues 14−16, 25−28, 37−40, 49−52, and 61−64. Disulfide bonds, shown in red, are located across each loop and between loops 1 and 2 at the N-terminus. (B) is rotated 90° to the left to emphasize the relative flatness of the proposed ice-binding face and (C) shows the view down the helix axis.

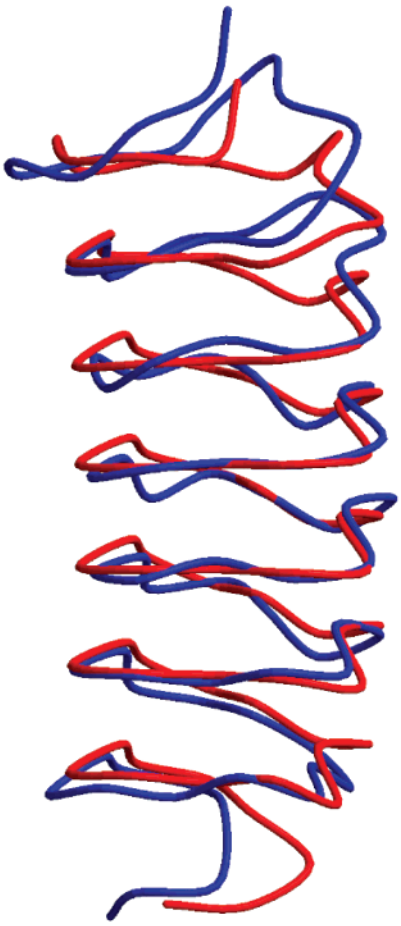

FIGURE 5: NMR and X-ray crystallographic structures of TmAFP. Shown are superimposed backbone traces of TmAFP solution (blue) and crystal (red) structures. The superimposition is for residues 13−81 with an rmsd of 1.35 Å. The view is the same as in Figure 4A.

all heavy atoms of the six well-defined loops as described above. The main difference is again in the N-terminal region, which is loosely defined in the solution structure. When the four C-terminal loops (residues 37−81) are used for superimposition, the rmsd between the two structures for the six well-defined loops drops to 1.1 Å for the backbone atoms; however, when the three N-terminal loops (from residues 10−37) are superimposed, the backbone rmsd is increased to 1.6 Å.

DYNAMIC RESULTS

^{15}N-T_1, -T_2, and NOE Data. The backbone dynamics of TmAFP have been studied at two temperatures, 30 and 5 °C. At 30 °C, 73 residues at 500 MHz and 75 residues at 600 MHz were used for the relaxation analysis, due to {^{1}H-^{15}N}-HSQC spectral overlap. At 5 °C, 72 residues at 500 MHz and 73 residues at 600 MHz were used.

The values of ^{15}N-T_1, -T_2, and {^{1}H}-^{15}N NOE as a function of residue number are shown for 30 °C in Figure 6 and for 5 °C in Figure 7. The profiles of ^{15}N-T_1, -T_2, and {^{1}H}-^{15}N NOE values for the two resonance frequencies display similar patterns as a function of residue number. The regular periodic pattern of the T_1, T_2, and T_1/T_2 values is obvious, corresponding to the 12-amino acid repeat sequence and loop structure. For proteins with $\tau_m \geq 5$ ns (i.e., in the slow tumbling limit), ^{15}N-T_1 values are largely dependent on the rates of motion occurring at the ^{15}N Larmor frequency, and

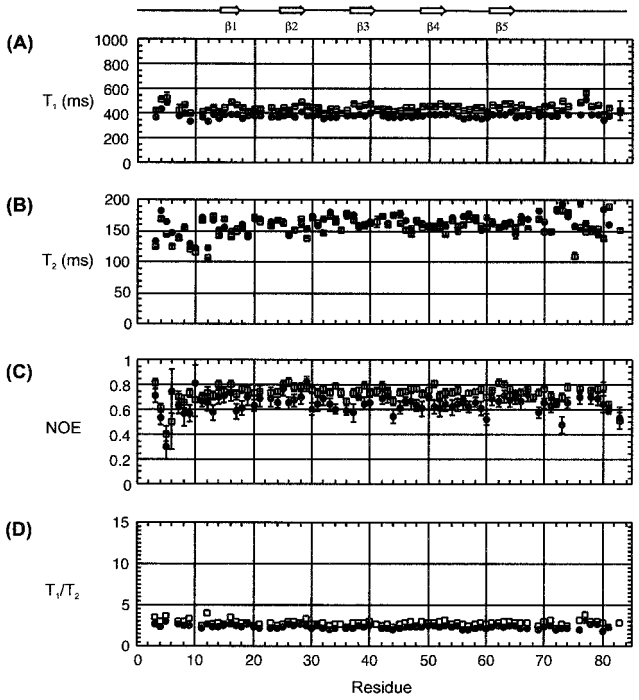

FIGURE 6: Plots of (A) ^{15}N-T_1, (B) ^{15}N-T_2, (C) {^{1}H}-^{15}N NOE, and (D) T_1/T_2 ratios at 30 °C with individual error bars plotted for 500 (●) and 600 (□) MHz. Average T_1/T_2 ratios calculated for residues with negligible internal motion (NOE > 0.6 (500 MHz) or NOE > 0.65 (600 MHz) were 2.36 ± 0.21 for T_1^{500}/T_2^{500} (●) and 2.84 ± 0.29 for T_1^{600}/T_2^{600} (□). A schematic diagram of secondary structure is drawn above the panel with arrows depicting the β-strands. The residues in structured regions are: β1 (14−16), β2 (25−28), β3 (37−40), β4 (49−52), and β5 (61−64).

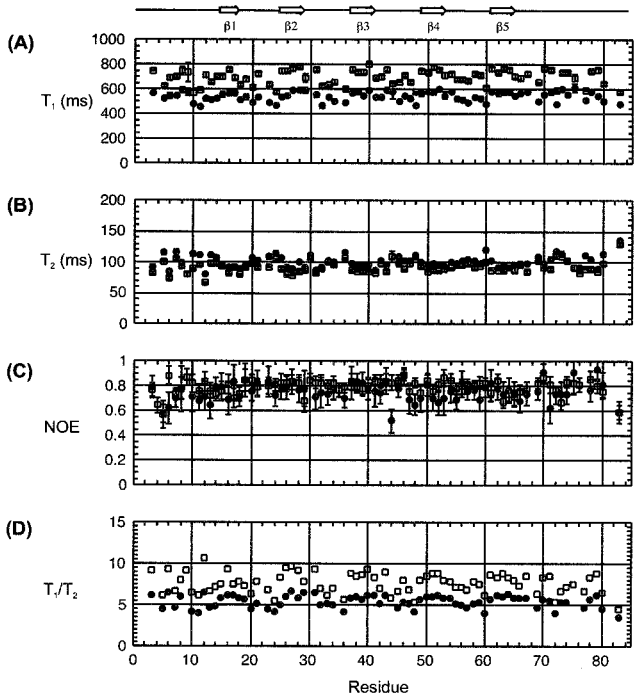

FIGURE 7: Plots of (A) ^{15}N-T_1, (B) ^{15}N-T_2, (C) {^{1}H}-^{15}N NOE, and (D) T_1/T_2 ratios at 5 °C with individual error bars plotted for 500 (●) and 600 (□) MHz. Average T_1/T_2 ratios calculated for residues with negligible internal motion (NOE > 0.6 (500 MHz) or NOE > 0.65 (600 MHz) were 5.46 ± 0.72 for T_1^{500}/T_2^{500} (●) and 7.75 ± 1.18 for T_1^{600}/T_2^{600} (□).

therefore exhibit characteristic magnetic field strength dependence (Figure 6). At 30 °C the T_1^{500} is 381 ± 22 ms

with an average error of 7 ms, and T_1^{600} is 445 ± 27 ms with an average error of 7 ms for all residues. The magnetic field strength dependence becomes more obvious at 5 °C (Figure 7) where the T_1^{500} is 542 ± 39 ms with an average error of 14 ms, and T_1^{600} is 695 ± 59 ms with an average error of 14 ms over all residues. ^{15}N-T_2 values in the slow tumbling limit are largely determined by the zero frequency value of the spectral density, $J(0)$, and are therefore expected to be similar at the different magnetic field strengths, as long as there are no chemical or conformational exchange contributions to T_2. At 30 °C, the average T_2^{500} is 162 ± 14 ms with an average error of 3 ms, and T_2^{600} is 156 ± 16 ms with an average error of 2 ms. At 5 °C these values drop as expected due to slower tumbling and the average T_2^{500} is 101 ± 10 ms with an average error of 2 ms, and T_2^{600} is 92 ± 10 ms with an average error of 2 ms over all residues. {^{1}H}-^{15}N NOE measurements are particularly sensitive to fast internal motions on the picosecond time scale ($0 < \tau_e < \tau_m$), and again a similar pattern is observed at the two magnetic field strengths as a function of residue number. At 30 °C, the average NOE^{500} is 0.65 ± 0.07 with an average error of 0.06 and NOE^{600} is 0.74 ± 0.05 with an average error of 0.04 for all residues. At 5 °C, the pattern holds and NOE^{500} is 0.75 ± 0.08 with an average error of 0.10 and NOE^{600} is 0.80 ± 0.06 with an average error of 0.06 over all residues.

Rotational Diffusion Anisotropy and Overall Correlation Time. To calculate the global τ_m, the first step is to remove residues with NOE values below a certain threshold. This is done because the NOE is sensitive to internal dynamics on the picosecond−nanosecond time-scale, and those residues with motions that are faster than τ_m on this time-scale must be eliminated prior to the calculation. An NOE cutoff value of 0.6 was used at 500 MHz and an NOE value of 0.65 was used at 600 MHz. A total of 56 out of 73 residues (30 °C) and 68 out of 72 residues (5 °C) from the 500 MHz data and 70 out of 75 residues (30 °C) and 70 out of 73 residues (5 °C) from the 600 MHz data set were selected by the NOE criteria for use in the global τ_m calculation. Residues that were removed from the data sets were typically from the N- and C-terminal regions of the protein.

Those residues that did not have their T_1/T_2 ratios excluded due to the NOE criteria described above were used to estimate the global τ_m. Residues with a T_1/T_2 ratio above or below one standard deviation of the mean for all residues were also removed. The relaxation parameters for each magnetic field strength were analyzed individually. At 30 °C, the average T_1/T_2 ratios of the selected residues are 2.36 ± 0.21 and 2.84 ± 0.29 at 500 and 600 MHz, respectively, while at 5 °C the T_1/T_2 ratios are 5.46 ± 0.72 and 7.75 ± 1.18 at 500 and 600 MHz. A total of 42 residues (30 °C) or 41 residues (5 °C) were used to calculate the global τ_m at 500 MHz, while a total of 53 residues (30 °C) or 48 residues (5 °C) were used at 600 MHz. τ_m was calculated on a per residue basis using the spectral density model 2 (eq 4) for isotropic rotational diffusion and the results were averaged to give the global τ_m. Global τ_m values of 4.2 ns (500 MHz) and 4.0 ns (600 MHz) were obtained at 30 °C. At 5 °C, a global τ_m of 7.7 ns was obtained at 500 MHz and 7.9 ns at 600 MHz.

From the observation of the periodic pattern of the raw dynamic data, anisotropy in the rotational tumbling of TmAFP is postulated. The crystal structure of TmAFP was used to calculate the normalized lengths of the principal axes of the inertia tensor, and the ratio was 1.00:0.52:0.45. Thus, anisotropy in the tumbling is indeed expected. The rotational diffusion anisotropy was examined for all residues not affected by large-amplitude fast picosecond and slower millisecond time-scale motions, in a manner similar to the procedure described by Pawley et al. (*51*). The relaxation parameters T_1, T_2, and NOE were analyzed with respect to isotropic, axially symmetric, and fully asymmetric rotational tumbling models using a grid search to find the minimum in the squared difference measured and calculated T_1/T_2 ratios using an in-house written program (*48*). All residues for which relaxation data was available were considered for the anisotropic rotational tumbling analysis, unless they were shown to be subject to significant internal motions, as determined by the filtering method above. The rotational tumbling of TmAFP is best characterized using the axially symmetric model with $D_{||}/D_\perp \cong 1.45$ at 30 °C and $D_{||}/D_\perp \cong 1.65$ at 5 °C for both magnetic field strengths (Table 2). A statistical *F*-test, shown in Table 2, validated the inclusion of additional parameters in the axially symmetric rotational diffusion model, while the fully asymmetric model was over-parametrized (*52*). For the axially symmetric model, the probability that the improvement in fit by the inclusion of additional parameters occurred by chance is 0 at 5 °C for both magnetic fields, and 3.2×10^{-11} (500 MHz) or 2.2×10^{-13} (600 MHz) at 30 °C. The axially symmetric rotational diffusion tensor was found to be prolate in shape ($D_{||}/D_\perp > 1$).

The orientation of the diffusion tensor with respect to the molecular structure of TmAFP is shown in Figure 8. D_z (or $D_{||}$), the unique axis of the rotational diffusion tensor, is parallel to the long axis of the β-helix. The orientation of the amide bond vectors of the backbone varies depending on which of the 12 positions in the loop it occupies. As will be expanded upon in the next section, this analysis was carried out to prevent the misinterpretation of relaxation parameters by the assumption of isotropic rotational diffusion in the internal mobility (model-free) analysis.

Model-Free Analysis and Internal Mobility. The Lipari-Szabo model-free approach (*41, 42*) is widely used to interpret backbone amide ^{15}N relaxation parameters. The experimental ^{15}N-T_1, -T_2, and {^{1}H}-^{15}N NOE relaxation parameters were fit to spectral density models 1−5. The spectral density parameters from each data set (500 and 600 MHz, at both 30 and 5 °C) were optimized individually (Figure 9) to allow assessment of the consistency between magnetic field strengths. This is possible to do since the motions that give rise to NMR relaxation are not dependent on magnetic field strengths, except for a slight alignment at higher magnetic field strengths (*53*).

The S^2 values obtained agree very well between the two magnetic field strengths, as expected. At 30 °C, the average S^2 values for the whole protein backbone are 0.87 at 500 MHz and 0.88 at 600 MHz (Figure 9A). These S^2 values are typical of well-defined secondary structure in proteins. At 5 °C, the average S^2 values are almost identical, 0.88 at 500 MHz and 0.89 at 600 MHz (Figure 9B). Only some residues in the N-terminal loop and the very C-terminal residues display any motion of varying amplitudes and rates. For TmAFP, both the β-sheet and extended loop regions of

Table 2: Rotational Diffusion Parameters by Isotropic, Axially Symmetric, and Asymmetric Models at 500 and 600 MHz and Two Temperatures (30 and 5 °C) for TmAFP[a]

model/field/temp	τ_m[b] (ns)	$D_{\|\|}/D_\perp$[c]	D_x/D_y	θ[d]	ϕ[d]	φ[d]	E[e]	E_v[f]	F_x[g]
isotropic[h]									
500 (30 °C)	4.2	1	1				709.4	11.4	
600 (30 °C)	4.0	1	1				2274.4	35.5	
500 (5 °C)	7.7	1	1				1442.2	22.9	
600 (5 °C)	7.9	1	1				2584.1	38.6	
ax. sym[h]									
500 (30 °C)	3.9	1.43	1	61.2	−133.6		292.1	4.9	28.1
600 (30 °C)	3.8	1.50	1	62.8	−130.8		813.8	13.3	36.5
500 (5 °C)	7.1	1.65	1	60.2	−120.6		194.9	3.2	128.0
600 (5 °C)	7.3	1.64	1	58.5	−121.0		474.3	7.4	94.9
asym[h]									
500 (30 °C)	4.0	1.38	0.87	62.2	−132.1	−24.2	282.1	4.9	1.0
600 (30 °C)	3.8	1.51	0.94	62.4	−131.7	−112.9	808.4	13.7	0.2
500 (5 °C)	7.1	1.67	0.94	60.7	−121.3	−44.4	193.1	3.3	0.3
600 (5 °C)	7.3	1.64	0.99	58.4	−121.0	0.1	474.1	7.6	0.01

[a] Values were calculated using the crystal structure of TmAFP (PDB entry 1EZG). [b] $\tau_m = 1/6D$. [c] $D_{||}/D_\perp = 2D_z/(D_x + D_y)$. [d] Euler angles describing the orientation of the components of the diffusion tensors, $D_z(\theta$ and $\phi)$ and $D_{x,y}(\varphi)$. [e] Error function $E = \sum_N (T_{1,e}/T_{2,e} - T_{1,c}/T_{2,c})^2/\sigma^2_{T_1/T_2}$, where N is the number of residues used in the fit. [f] Reduced error function $E_v = E/(N - m)$, where N and m are the number of residues and variables used in the fit, respectively. [g] $F_x = (E_m - E_{m+x})/xE_{v,m+x}$, where E and E_v are defined above and x is the number of additional variables in the fit. Larger F_x values justify the use of additional variables (*48*). [h] For the isotropic, axially symmetric, and fully asymmetric anisotropic analyses, 63 (30 °C) and 64 (5 °C) residues at 500 MHz and 65 (30 °C) and 68 (5 °C) residues at 600 MHz were used.

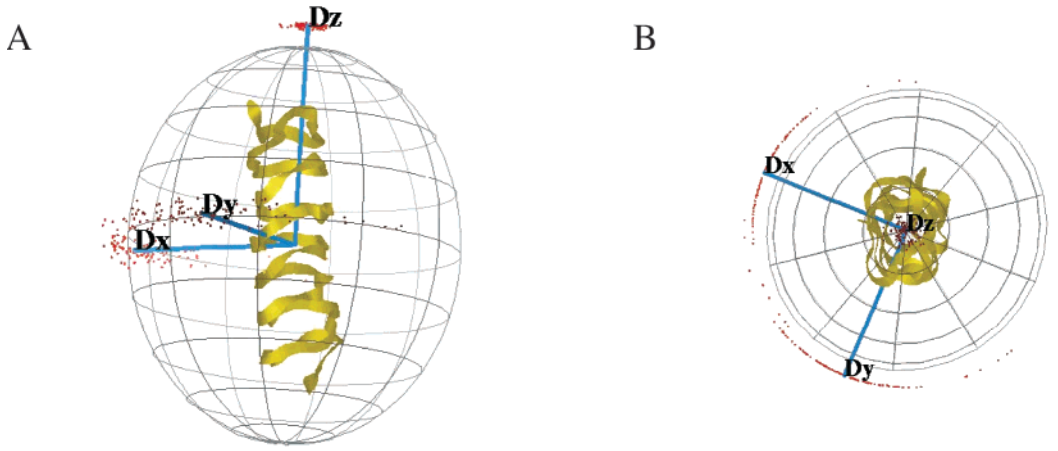

FIGURE 8: Rotational diffusion tensor of TmAFP. The best fit rotational diffusion tensor of TmAFP is shown superimposed on the TmAFP structure closest to the mean. The tensor is visualized as a three-dimensional ellipsoid with its axes marked. The orientation of the molecule in (A) is the same as in Figure 4B, while (B) shows the view down the helix axis from the position in (A).

the protein are highly structured.

All of the model-free analysis was performed accounting for rotational diffusion anisotropy (eq 9), as the failure to include this will lead to misidentification of τ_e and/or R_{ex} terms as genuine slow motions and conformational exchange (*46*). As well, S^2 values calculated assuming isotropic rotational diffusion are also affected and appear artificially lowered, implying the molecule is more flexible and undergoes more internal motion than is actually occurring. For TmAFP, as shown in Figure 8, D_z ($D_{||}$) is parallel to the long axis of the β-helix. Around each loop of the helix, the orientations of the N−NH bond vector in each of the 12 positions vary from parallel to the helical axis to nearly perpendicular. These different orientations with respect to the unique axis of the diffusion tensor are what give rise to the periodic pattern displayed by the experimental relaxation data.

DISCUSSION

The study of protein backbone dynamics provides detailed and site-specific information about the conformational changes that can occur upon ligand binding. Nuclear magnetic resonance spectroscopy is sensitive to a wide range of motions of various time scales, and is particularly applicable to this type of dynamic study. For TmAFP, the proposed ice-binding region is the array of threonine residues that form the parallel β-sheet on one face of the protein (*16*). The parameters extracted from these ^{15}N NMR relaxation studies show that TmAFP has similar restricted internal mobility throughout the protein backbone, at both temperatures studied. Therefore, both the ice-binding and opposite faces of TmAFP are formed by well-defined and rigid structural elements and the overall backbone dynamics are not affected as TmAFP approaches its physiologically relevant temperature.

This observed backbone rigidity of the ligand binding site is a recurring theme in several recent publications (*54*, *55*), in contrast to observations that ligand binding is often related to increased active site flexibility (*56*). In other recent studies, the heteronuclear NMR spin relaxation data has been interpreted in terms of its contributions to protein entropy and heat capacity (*57*). In the case of TmAFP, the ligand it

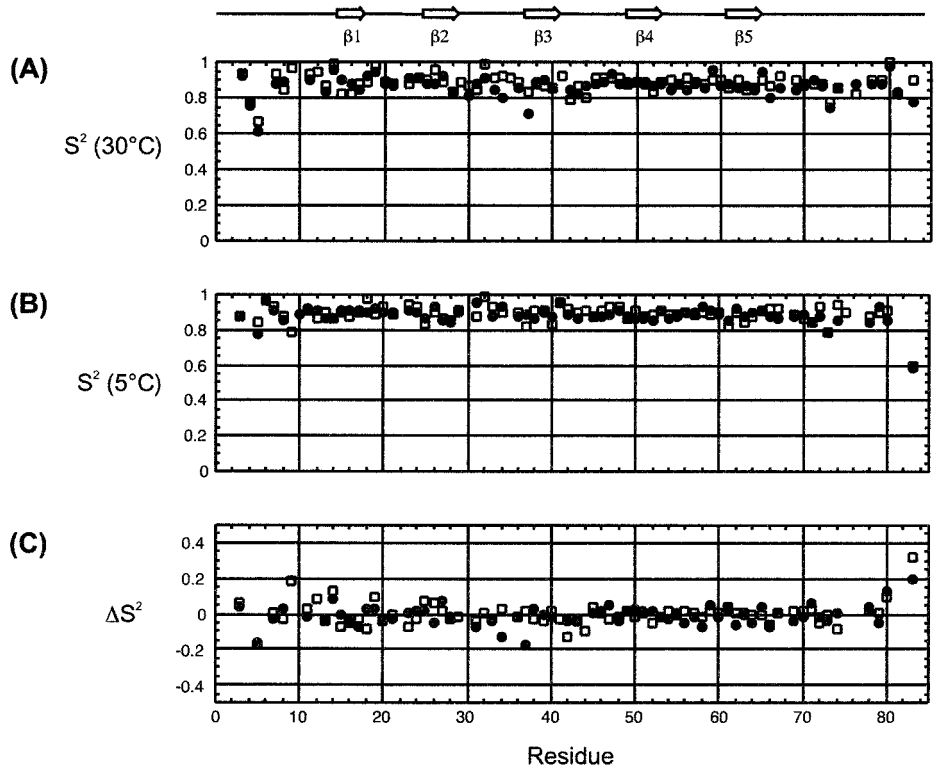

FIGURE 9: Plots of (A) order parameters (S^2) at 30 °C, (B) S^2 at 5 °C, and (C) $\Delta S^2 = S^2(30\ °C) - S^2(5\ °C)$ for 500 (●) and 600 (□) MHz data.

binds is ice, which has an extremely regular spacing of its repetitive elements. If lattice matching to this array is to occur, it follows that the binding site in question would be rigid to ensure the correct positioning of the required protein constituents in close proximity. For TmAFP, we propose that the hydrophobic, rigid binding site reduces the entropic penalty for the free energy of binding the protein to ice.

An examination of the structure of TmAFP suggests that a β-helix provides an ideal scaffold to produce the required rigidity of the ice-binding site. Although parallel β-helix structures have been discovered in bacteria and fungi, including other right-handed β-helices such as pectate lyase (*58*), rhamnogalacturonase A (*59*), and the P22 tailspike protein (*60*), and the left-handed β-helix domain of *N*-acetylglucosamine acyltransferase (*61*), all these proteins are much larger and less strictly regular than TmAFP. They typically contain 22 to 27 residues per β-helical loop, and all have normal hydrophobic cores. Since no dynamic studies on these larger β-helices have been undertaken, we cannot state whether these β-helices will also demonstrate a similar degree of rigidity, although it is certainly a distinct possibility. Nonetheless, the compact size and shape of the TmAFP β-helix as compared to other β-helical structures, coupled with the extensive disulfide- and hydrogen-bonding, structures the helical loops to such a high degree that even the lack of a hydrophobic core does not affect its stability. It is interesting to note that another insect AFP, that of spruce budworm, has utilized a β-helical structure with a triangular architecture as a scaffold for antifreeze activity (*17*), while β-helical structures have also been postulated for the leucine-rich carrot AFP (*3*) and recently characterized ryegrass AFP (*62*). However, a β-helical AFP structure has not yet been seen in fishes.

In conclusion, we have determined that the entire TmAFP molecule is a highly structured and rigid protein. This rigidity appears to be inherent in the β-helical structure and does not appear to be a consequence of the lowering of the solution temperature toward physiologically active temperatures. From this observation, we suggest that the β-helix structure is an ideal scaffold for antifreeze protein activity and the key element to its success is its repetitive structure and associated rigidity, which allows it to match the solid ice crystal lattice as it binds. Given the wide variety of observed AFP structures in fish, it would be informative to study backbone dynamics of these AFPs to compare their proposed ice-binding face dynamics. As well, since it is clear that side chains play very important roles in binding interfaces, a detailed look at their dynamic behavior will be the next logical step in the attempt to elucidate the molecular mechanism of antifreeze protein binding to ice.

ACKNOWLEDGMENT

We thank Dr. Steffen Graether and Dr. Carolyn Slupsky for helpful discussions and suggestions; Professor Lewis E. Kay for providing pulse sequences; Pascal Mercier and Dr. Stéphane Gagné for useful software programs and scripts; Gerry McQuaid for maintenance of the NMR spectrometers; Sherry Gauthier and Yih-Cherng Liou for protein expression; and Robert Boyko and Leigh Willard for computer expertise. We would also like to thank the Canadian National High Field NMR Centre (NANUC) for their assistance and use of the facilities. The operation of NANUC is funded by the Canadian Institutes of Health Research, the Natural Science and Engineering Research Council of Canada and the University of Alberta.

SUPPORTING INFORMATION AVAILABLE

Supporting Information available includes the ^{15}N and ^{1}H chemical shift assignments for the backbone and side-chains of TmAFP. This material is available free of charge via the Internet at http://pubs.acs.org.

REFERENCES

1. Fletcher, G. L., Hew, C. L., and Davies, P. L. (2001) *Annu. Rev. Physiol. 63*, 359−390.
2. Duman, J. G. (2001) *Annu. Rev. Physiol. 63*, 327−357.
3. Worrall, D., Elias, L., Ashford, D., Smallwood, M., Sidebottom, C., Lillford, P., Telford, J., Holt, C., and Bowles, D. (1998) *Science 282*, 115−117.
4. Sidebottom, C., Buckley, S., Pudney, P., Twigg, S., Jarman, C., Holt, C., Telford, J., McArthur, A., Worrall, D., Hubbard, R., and Lillford, P. (2000) *Nature 406*, 249−251.
5. Graham, L. A., Liou, Y.-C., Walker, V. K., and Davies, P. L. (1997) *Nature 388*, 727−728.
6. Tyshenko, M. G., Doucet, D., Davies, P. L., and Walker, V. K. (1997) *Nat. Biotechnol. 15*, 887−890.
7. DeVries, A. L., and Wohlschlag, D. E. (1969) *Science 163*, 1073−1075.
8. Grimstone, A. V., Mullinger, A. M., and Ramsay, J. A. (1968) *Philos. Trans. R. Soc. London B 253*, 343−382.
9. Davies, P. L., and Sykes, B. D. (1997) *Curr. Opin. Struct. Biol. 7*, 828−834.
10. Yeh, Y., and Feeney, R. E. (1996) *Chem. Rev. 96*, 601−617.
11. Yang, D. S., Sax, M., Chakrabartty, A., and Hew, C. L. (1988) *Nature 333*, 232−237.
12. Gronwald, W., Loewen, M. C., Lix, B., Daugulis, A. J., Sonnichsen, F. D., Davies, P. L., and Sykes, B. D. (1998) *Biochemistry 37*, 4712−4721.
13. Sonnichsen, F. D., DeLuca, C. I., Davies, P. L., and Sykes, B. D. (1996) *Structure 4*, 1325−1337.
14. Jia, Z., DeLuca, C. I., Chao, H., and Davies, P. L. (1996) *Nature 384*, 285−288.
15. Deng, G., Andrews, D. W., and Laursen, R. A. (1997) *FEBS Lett. 402*, 17−20.
16. Liou, Y.-C., Tocilj, A., Davies, P. L., and Jia, Z. (2000) *Nature 406*, 322−324.
17. Graether, S. P., Kuiper, M. J., Gagné, S. M., Walker, V. K., Jia, Z., Sykes, B. D., and Davies, P. L. (2000) *Nature 406*, 325−328.
18. Chao, H., Houston, M. E., Jr., Hodges, R. S., Kay, C. M., Sykes, B. D., Loewen, M. C., Davies, P. L., and Sonnichsen, F. D. (1997) *Biochemistry 36*, 14652−14660.
19. Haymet, A. D. J., Ward, L. G., Harding, M. M., and Knight, C. A. (1998) *FEBS Lett. 430*, 301−306.
20. Zhang, W., and Laursen, R. A. (1998) *J. Biol. Chem. 273*, 34806−34812.
21. Haymet, A. D. J., Ward, L. G., and Harding, M. M. (1999) *J. Am. Chem. Soc. 121*, 941−948.
22. Baardsnes, J., Kondejewski, L. H., Hodges, R. S., Chao, H., Kay, C. M., and Davies, P. L. (1999) *FEBS Lett. 463*, 87−91.
23. Chao, H., Sonnichsen, F. D., DeLuca, C. I., Sykes, B. D., and Davies, P. L. (1994) *Protein Sci. 3*, 1760−1769.
24. Knight, C. A., Cheng, C. C., and DeVries, A. L. (1991) *Biophys. J. 59*, 409−418.
25. Kay, L. E. (1998) *Nat. Struct. Biol. 5 (Suppl.)*, 513−517.
26. Ishima, R., and Torchia, D. A. (2000) *Nat. Struct. Biol. 7*, 740−743.
27. Graether, S. P., Slupsky, C. M., Davies, P. L., and Sykes, B. D. (2001) *Biophys. J. 81*, 1677−1683.
28. Lane, A. N., Hays, L. M., Tsvetkova, N., Feeney, R. E., Crowe, L. M., and Crowe, J. H. (2000) *Biophys. J. 78*, 3195−3207.
29. Liou, Y.-C., Daley, M. E., Graham, L. A., Kay, C. M., Walker, V. K., Sykes, B. D., and Davies, P. L. (2000) *Protein Exp. Purif. 19*, 148−157.
30. Delaglio, F., Grzesiek, S., Vuister, G. W., Zhu, G., Pfeifer, J., and Bax, A. (1995) *J. Biomol. NMR 6*, 277−293.
31. Johnson, B. A., and Blevins, R. A. (1994) *J. Biomol. NMR 4*, 603−614.
32. Brünger, A. T., Adams, P. D., Clore, G. M., DeLano, W. L., Gros, P., Grosse-Kunstleve, R. W., Jiang, J.-S., Kuszewski, J., Nilges, M., Pannu, N. S., Read, R. J., Rice, L. M., Simonson, T., and Warren, G. L. (1998) *Acta Crystallogr. D 54*, 905−921.
33. Vuister, G. W., and Bax, A. (1993) *J. Am. Chem. Soc. 115*, 7772−7777.
34. Gagné, S. M., Tsuda, S., Li, M. X., Chandra, M., Smillie, L. B., and Sykes, B. D. (1994) *Protein Sci. 3*, 1961−1974.
35. Laskowski, R. A., Rullmann, J. A. C., MacArthur, M. W., Kaptein, R., and Thornton, J. M. (1996) *J. Biomol. NMR 8*, 477−486.
36. Willard, L., Wishart, D. S., and Sykes, B. D. (1997) *VADAR Version 1.2*, University of Alberta, Edmonton, Alberta, Canada.
37. Kraulis, P. J. (1991) *J. Appl. Crystallogr. 24*, 946−950.
38. Merritt, E. A., and Bacon, D. J. (1997) *Methods Enzymol. 277*, 505−524.
39. Farrow, N. A., Muhandiram, R., Singer, A. U., Pascal, S. M., Kay, C. M., Gish, G., Shoelson, S. E., Pawson, T., Forman-Kay, J. D., and Kay, L. E. (1994) *Biochemistry 33*, 5984−6003.
40. Abragam, A. (1961) *Principles of Nuclear Magnetism*, Clarendon Press, Oxford, U.K.
41. Lipari, G., and Szabo, A. (1982) *J. Am. Chem. Soc. 104*, 4546−4559.
42. Lipari, G., and Szabo, A. (1982) *J. Am. Chem. Soc. 104*, 4559−4570.
43. Clore, G. M., Szabo, A., Bax, A., Kay, L. E., Driscoll, P. C., and Gronenborn, A. M. (1990) *J. Am. Chem. Soc. 112*, 4989−4991.
44. Clore, G. M., Driscoll, P. C., Wingfield, P. T., and Gronenborn, A. M. (1990) *Biochemistry 29*, 7387−7401.
45. Woessner, D. E. (1962) *J. Chem. Phys. 37*, 647−654.
46. Tjandra, N., Feller, S. E., Pastor, R. W., and Bax, A. (1995) *J. Am. Chem. Soc. 117*, 12562−12566.
47. Tjandra, N., Wingfield, P., Stahl, S., and Bax, A. (1996) *J. Biomol. NMR 8*, 273−284.
48. Gagné, S. M., Tsuda, S., Spyracopoulos, L., Kay, L. E., and Sykes, B. D. (1998) *J. Mol. Biol. 278*, 667−686.
49. Dosset, P., Hus, J. C., Blackledge, M., and Marion, D. (2000) *J. Biomol. NMR 16*, 23−28.
50. Liou, Y.-C., Thibault, P., Walker, V. K., Davies, P. L., and Graham, L. A. (1999) *Biochemistry 38*, 11415−11424.
51. Pawley, N. H., Wang, C., Koide, S., and Nicholson, L. K. (2001) *J. Biomol. NMR 20*, 149−165.
52. Bevington, P. R., and Robinson, D. K. (1992) *Data Reduction and Error Analysis for the Physical Sciences*, 2nd ed.; McGraw-Hill, New York.
53. Tjandra, N., Grzesiek, S., and Bax, A. (1996) *J. Am. Chem. Soc. 118*, 6264−6272.
54. Suh, J.-Y., Spyracopoulos, L., Keizer, D. W., Irvin, R. T., and Sykes, B. D. (2001) *Biochemistry 40*, 3985−3995.
55. Poget, S. F., Freund, S. M. V., Howard, M. J., and Bycroft, M. (2001) *Biochemistry 40*, 10966−10972.
56. Forman-Kay, J. D. (1999) *Nat. Struct. Biol. 6*, 1086−1087.
57. Spyracopoulos, L., and Sykes, B. D. (2001) *Curr. Opin. Struct. Biol. 11*, 555−559.
58. Yoder, M. D., Keen, N. T., and Jurnak, F. (1993) *Science 260*, 1503−1507.
59. Petersen, T. N., Kauppinen, S., and Larsen, S. (1997) *Structure 5*, 533−544.
60. Steinbacher, S., Seckler, R., Miller, S., Steipe, B., Huber, R., and Reinemer, P. (1994) *Science 265*, 383−386.
61. Raetz, C. R., and Roderick, S. L. (1995) *Science 270*, 997−1000.
62. Kuiper, M. J., Davies, P. L., and Walker, V. K. (2001) *Biophys. J. 81*, 3560−3565.

BI0121252